



# A hybrid feature-based patient-to-image registration method for robot-assisted long bone osteotomy

Chunlei Zhang<sup>1</sup> · Yu Liu<sup>1</sup> · Yunguang Zhang<sup>2</sup> · He Li<sup>1</sup>

Received: 30 January 2021 / Accepted: 17 June 2021 / Published online: 26 June 2021  
© CARS 2021

## Abstract

**Purpose** The purpose of this study is to provide a simple, feasible and effective patient-to-image registration method for robot-assisted long bone osteotomy, which has rarely been systematically reported. The practical requirement is to meet the accuracy of 1 mm or even higher without bone-implanted markers.

**Methods** A hybrid feature-based registration method termed CR-RAMSICP is proposed. Point-based coarse registration (CR) is accomplished relying on the optical retro-reflective markers attached to the tracked rigid body fixed out of the bone. In surface-based fine registration, an improved iterative closest point (ICP) algorithm based on the range-adaptive matching strategy (termed RAMSICP) is presented to cope with the robust precise matching between the asymmetric patient and image point clouds, which avoids converging to a local minimum.

**Results** A series of registration experiments based on the isolated porcine iliums are carried out. The results illustrate that CR-RAMSICP not only significantly outperforms CR and CR-ICP in the accuracy and reproducibility, but also exhibits better robustness to the CR errors and less sensitiveness to the distribution and number of fiducial points located in the patient point cloud than CR-ICP.

**Conclusion** The proposed registration method CR-RAMSICP can stably satisfy the desired registration accuracy without the use of bone-implanted markers like fiducial screws. Besides, the RAMSICP algorithm used in fine registration is convenient for programming because any complex metrics or models are not involved.

**Keywords** Robot-assisted surgery · Orthopedic robot · Long bone osteotomy · Patient-to-image registration

## Introduction

Orthopedic robot systems (ORSs) have been widely applied to clinical surgery of knees, hips, spines, skulls, zygomas, maxillofacial, teeth, etc., greatly improving the safety, accuracy and efficiency of traditional artificial surgery [1–4]. During ORS-assisted surgery, surgical planning is first customized by the surgeon using medical images of patient's anatomy and then guides the robot system to perform the required manipulation tasks (e.g., osteotomy and target positioning). For this purpose, patient-to-image registration (hereinafter referred to as registration) is necessary, which

largely determines the surgical outcome. Its essence is to find a rigid transformation between the intra-operative patient's anatomy (called patient space) and the corresponding CT images (called image space) using an appropriate registration method [5]. Generally, marker-based paired-point registration (MBPPR) and surface-based marker-less registration (SBMLR) methods have been developed to adapt to different surgical objects, conditions and procedures [6, 7].

MBPPR is commonly acknowledged to be high-accuracy [8, 9]. No fewer than three non-collinear artificial markers which significantly differ from patient's anatomy in X-ray absorptivity, are frequently inserted into the bone [10–12], or fixed out of patient's anatomy with an extending bracket [3], or glued onto the skin surface [13]. The paired fiducial points (FPs) in patient and image spaces determined by these markers can be manually or automatically obtained [14], and then the transformation between them can be solved by the representative least-squares fitting method [15]. However, MBPPR faces several practical challenges

✉ Yu Liu  
yuliu@me.neu.edu.cn

<sup>1</sup> School of Mechanical Engineering and Automation, Northeastern University, Shenyang, China

<sup>2</sup> Shenyang Xingwen Technology Co., Ltd, Shenyang, China

involving: introducing invasive bone-implanted markers not only requires time-consuming preparation, but also causes discomfort even complications to patients [11]; skin-adhered markers may slip or fall off, which negatively impacts the registration accuracy [5]; the target registration error (TRE) may be significantly amplified with the distance between the external markers and the patient's anatomy [3]; artifacts of metal markers produced in CT images severely limit the segmentation and detection of markers [16].

Accordingly, SBMLR attracts more attention. The patient point cloud (PPC) acquired from the anatomic surfaces using a scanner, or a stereo camera [6, 17–20], or a digital touch probe [9, 11, 21] is frequently registered to the corresponding image point cloud (IPC) extracted from the CT images via the most representative iterative closest point (ICP) algorithm [22]. Generally, the PPC acquired by scanners or stereo cameras contains tens to hundreds of thousands densely distributed FPs to characterize a relatively complete anatomic surface, which is closest to the IPC in the number of FPs, thus greatly increasing the computing time. Furthermore, numerous disturbances (e.g., noises, outliers) existing in the PPC and/or IPC, caused by the uncertainty of sampling and image segmentation of bone surface, have adverse effects on the registration accuracy and robustness. Some reported algorithms [23–26] aiming at solving similar issues require the establishments of complex metrics or models, which increase the calculation complexity and programming difficulty. In contrast, the PPC collected by successively touching the exposed bone surface using a digital touch probe, usually contains only fewer than one hundred sparsely distributed FPs due to the limited accessibility and operation time [6], which is seriously asymmetric to the IPC in the number and distribution. In this case, numerous FPs regarded as possible disturbances in the IPC that cannot accurately match with those in the PPC, which may lead to a wrong registration trend. Besides, another marker-less scheme is to pick up the paired anatomic landmarks in image and patient spaces [5, 27, 28].

The goal of this study is to provide a simple, feasible, robust and high-accuracy (i.e., the TRE is about 1 mm) registration scheme for robot-assisted long bone osteotomy, which has rarely been systematically reported to our knowledge. Other practical requirements mainly involve that (1) invasive bone-implanted and skin-adhered markers are undesirable; (2) the exposed bone surface should be as small as possible; (3) the intra-operative real-time registration and tracking performance of the patient's bone needs to be guaranteed; however, scanner-based and stereo camera-based schemes are usually subject to this limitation due to large amounts of data to be processed; (4) anatomic landmark-based method is not absolutely reliable because the long bone surfaces are usually too smooth to find distinguishing features.

Based on the consideration of the reported methods and practical requirements, we present a hybrid feature-based patient-to-image registration method termed CR-RAMSICP and integrate it into our self-developed ORS. In this paper, the ORS architecture is first outlined. Then, the proposed CR-RAMSICP is elaborated, in which coarse and fine registrations adopt different fiducial data and algorithms, respectively. The initial alignment between the PPC collected by the tracked optical probe and the IPC extracted from the CT datasets is accomplished, relying on the retro-reflective markers (RRMs) attached to the tracked rigid body which is rigidly fixed out of the bone with an extending bracket. The fine transformation between the PPC and the IPC is solved by an improved ICP algorithm based on the range-adaptive matching strategy (termed RAMSICP). Subsequently, we experimentally evaluate the accuracy of the proposed method and discuss some important impact factors. The registration results of isolated porcine iliums indicate that CR-RAMSICP is effective for accuracy improvement without bone-implanted markers, and exhibits great robustness to the CR errors, and low sensitivity to sampling with the tracked probe. Finally, the conclusions and prospects are given.

## Context

The self-developed ORS is modularized into tracking, patient, image and robot subsystems (see Fig. 1). A high-accuracy infrared optical tracking system (Polaris Vega®, NDI, Canada) is selected as the tracking subsystem, including a set of near-infrared (NIR) sensors, a tracked rigid body and a tracked probe. Each tracked tool is localized by multiple attached wireless RRM which can be tracked by the NIR sensors automatically. To construct the patient subsystem, the tracked rigid body is rigidly fixed out of an isolated porcine ilium (instead of a real patient) by inserting an extending bracket into the porcine ilium. Note that in clinical application, a special bone clip equipped on the extending bracket can avoid the invasiveness to a real patient. The image subsystem mainly provides an integrated surgical navigation software programmed by Python based on the open source software platform “3D Slicer” to guide the operation processes, which supports image processing, three-dimensional (3D) visualization, surgical planning, tool calibration, registration, intra-operative real-time navigation, etc. The developed software runs on a computer with an Intel (R) core (TM) i7-1065G7 (1.30 GHz) processor, 16 GB RAM, and the Windows 10 operating system. The robot subsystem is constructed by a six-degree-of-freedom robot (UR5, Universal Robots, Denmark) equipping a surgical tool, which can perform a full-automatic osteotomy process in strict accordance with the planned tool trajectory.

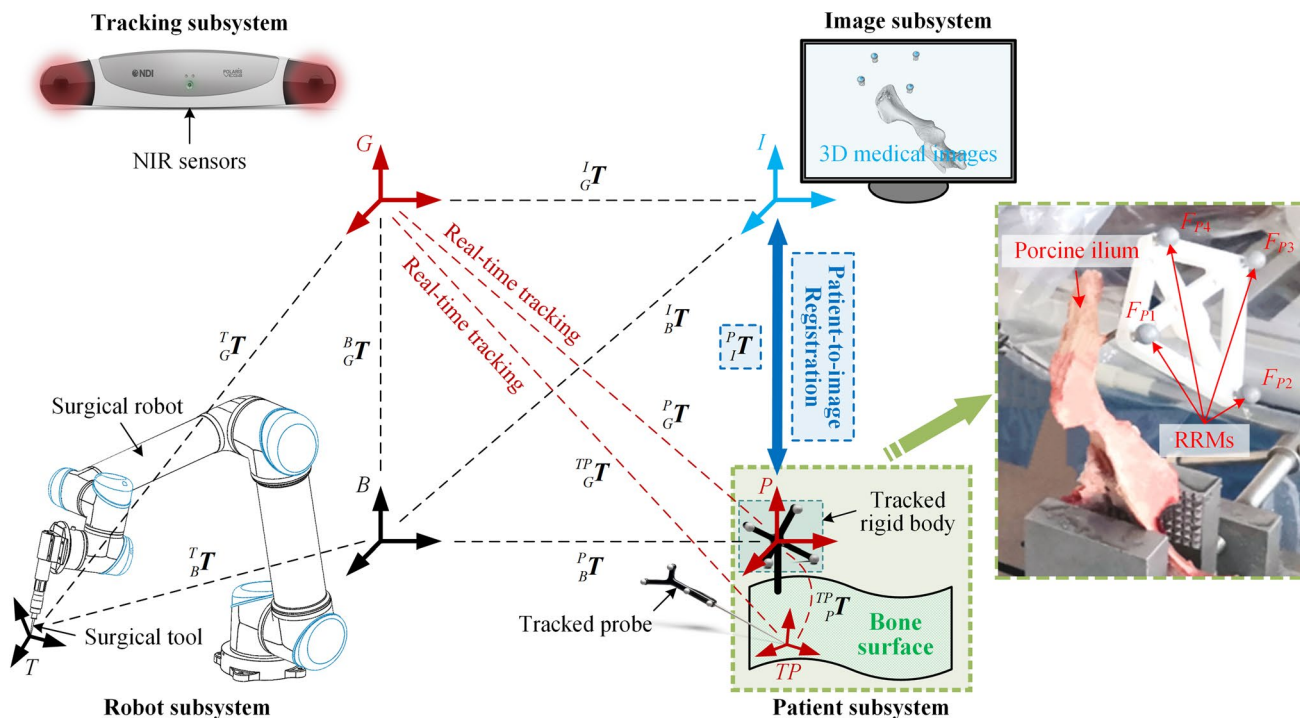


**Fig. 1** The self-developed ORS composition and the transformation relationships between CSs. *G*: global CS determined by the NIR sensors. *P*: patient CS determined by the RRM centers. *TP*: probe CS. *B*: robot base CS. *T*: surgical tool CS. *I*: image CS

Each rigid transformation between any two coordinate systems (CSs) determined by the corresponding subsystems is defined and illustrated in Fig. 1, and mathematically described by a homogeneous transformation matrix:

$${}_{\text{ref}}^{\text{tar}}\mathbf{T} = \begin{bmatrix} \mathbf{R}_{3 \times 3} & \mathbf{t}_{3 \times 1} \\ \mathbf{0}_{1 \times 3} & 1 \end{bmatrix}_{4 \times 4} = \begin{bmatrix} n_x & o_x & a_x & t_x \\ n_y & o_y & a_y & t_y \\ n_z & o_z & a_z & t_z \\ 0 & 0 & 0 & 1 \end{bmatrix} \quad (1)$$

where  ${}_{\text{ref}}^{\text{tar}}\mathbf{T}$  represents the transformation matrix from the reference CS *ref* to the target CS *tar* and  $\mathbf{R}$  and  $\mathbf{t}$  are the rotation matrix and translation vector of  ${}_{\text{ref}}^{\text{tar}}\mathbf{T}$ , respectively. The solution principles for several key matrices are briefly described as follows:

- (1)  ${}^P_G\mathbf{T}$  and  ${}^{TP}_G\mathbf{T}$  can be tracked by the NIR sensors directly, and then  ${}^{TP}_P\mathbf{T}$  can be calculated as follows:

$${}^{TP}_P\mathbf{T} = ({}^P_G\mathbf{T})^{-1} \cdot {}^{TP}_G\mathbf{T} \quad (2)$$

- (2)  ${}^T_B\mathbf{T}$  can be computed by combining the robot kinematics and the four-point calibration method [29].
- (3) To calculate  ${}^B_G\mathbf{T}$ , an optical calibrator was customized (see Fig. 2). First, the calibrator was installed on the surgical tool to ensure that the current tool center point  $p_{\text{tcp}}$  of the surgical tool coincides with the calibration groove bottom point  $p_{\text{gbp}}$  which can be directly tracked

by the NIR sensors. Their relative movement was constrained by a clamping device. Then, the tool center point was controlled by the robot to reach any three non-collinear positions  $p_1, p_2$  and  $p_3$  in turn which were used to establish the auxiliary CS *A*. Obviously,  ${}^A_B\mathbf{T}$  and  ${}^A_G\mathbf{T}$  are easy to determine, and thus  ${}^B_G\mathbf{T}$  can be calculated as follows:

$${}^B_G\mathbf{T} = {}^A_G\mathbf{T} \cdot ({}^A_B\mathbf{T})^{-1} \quad (3)$$

- (4) All surgical tool poses planned in image space should be eventually transmitted to the robot controller. Consequently,  ${}^B_I\mathbf{T}$  is necessary and can be calculated as follows:

$${}^B_I\mathbf{T} = ({}^B_G\mathbf{T})^{-1} \cdot {}^P_G\mathbf{T} \cdot ({}^P_I\mathbf{T})^{-1} \quad (4)$$

where  ${}^P_I\mathbf{T}$  represents the patient-to-image registration matrix to be solved by our proposed method.

### Hybrid feature-based registration

Figure 3 illustrates the main procedures of the proposed hybrid feature-based registration method.

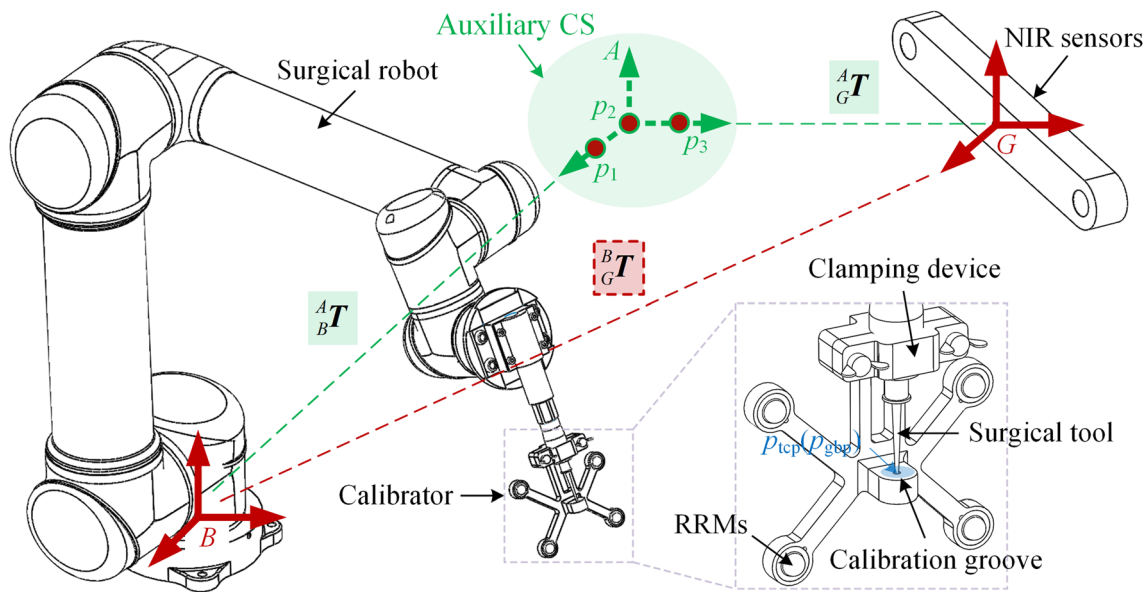


Fig. 2 Schematic diagram of calibration between the tracking and robot subsystems

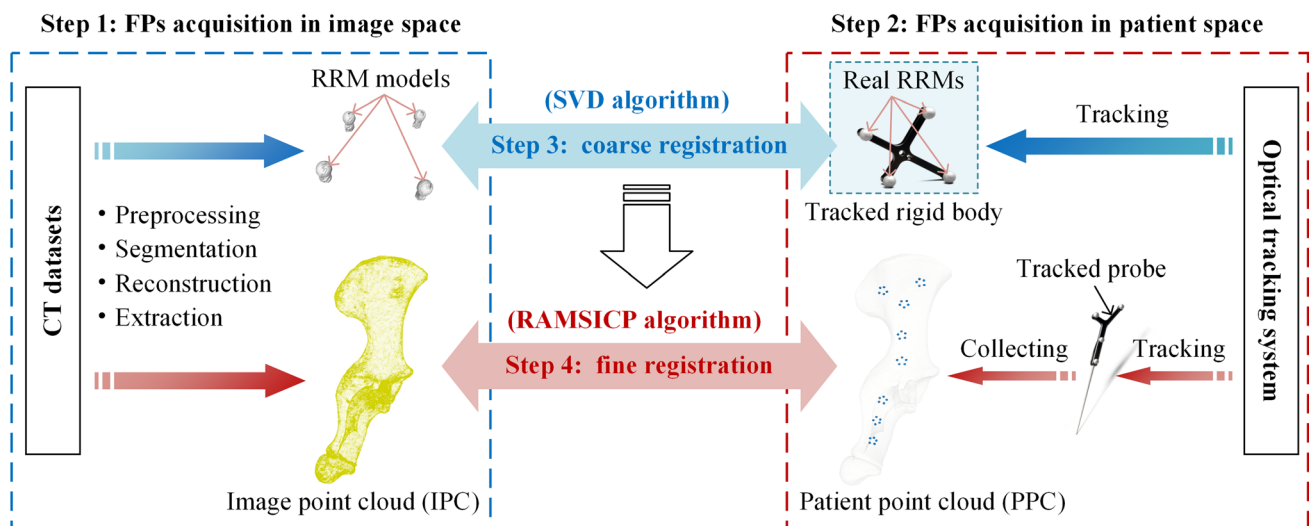
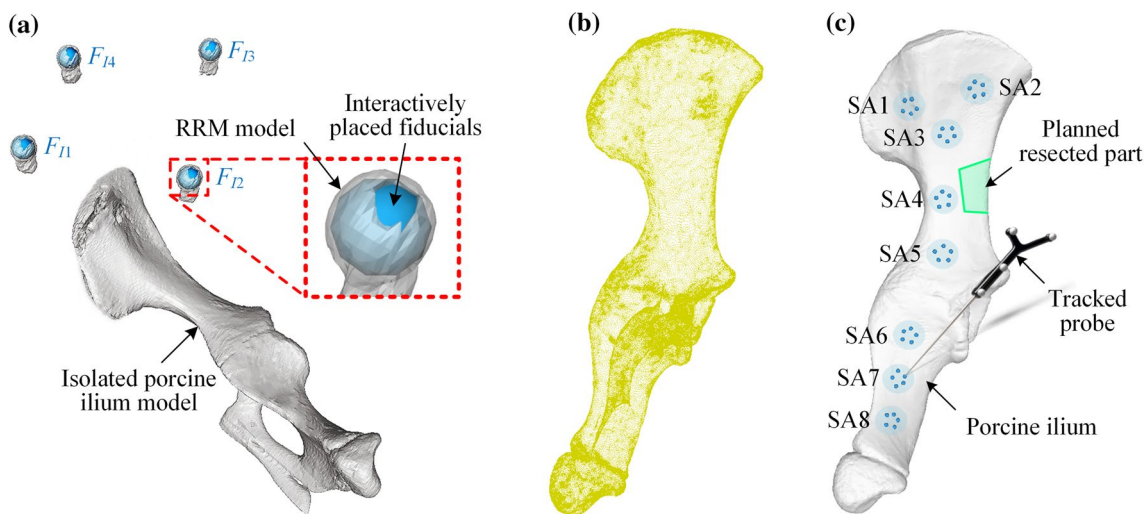


Fig. 3 Overview of the proposed method

## Data acquisition

- (1) *FPs acquisition in image space.* The CT datasets of the patient subsystem were first scanned by a C-arm (ARCADIS Varic, Siemens, Germany), characterized by a 0.625 mm slice thickness and a 0.5 mm pixel size, then were filtered and denoised. Next, four RRMs attached to the tracked rigid body and the isolated porcine ilium were segmented out using a threshold-based method [30], and Fig. 4a shows their reconstructed virtual models. Subsequently, the IPC (see Fig. 4b) was
- (2) *FPs acquisition in patient space.* Each FP was collected successively by a single touch of the porcine ilium surface with the tracked probe. These FPs were mapped into the patient CS using the transformation illustrated in Fig. 1 to compose the PPC, represented as  $X = \{x_i\}$  for  $i = 1, \dots, N_p$ , and their distribution pattern shown in Fig. 4c satisfies that (i) eight sub-areas (SAs) denoted as SA1-SA8 were set on the unilateral smooth surface



**Fig. 4** a 3D virtual model of the patient subsystem and placed virtual fiducials (blue points). b The IPC with 194 568 FPs. c The PPC with 40 FPs (blue points)

of the porcine ilium; (ii) each SA contains five randomly distributed FPs.

It should be clarified that during above-mentioned procedures, there must be no relative movement between the tracked rigid body and the porcine ilium. Besides, during clinical practice, the medical fixator attaching reference markers usually needs to be clamped on the real patient’s bone with a special bone clip intra-operatively, and thus intra-operative imaging is necessary, which provides better reliability and safety than pre-operative imaging.

**Coarse registration**

The RRM models can provide more reliable features than anatomic landmarks, and their geometric centers  $F_p = \{F_{P1}, F_{P2}, F_{P3}, F_{P4}\}$  (see Fig. 1) can be tracked and mapped into the patient CS automatically. In image space, four virtual spherical fiducials with the same 11.5 mm diameter as the real RRM models were interactively placed through the built-in tool “Fiducials” of 3D Slicer, and their centers  $F_I = \{F_{I1}, F_{I2}, F_{I3}, F_{I4}\}$  were adjusted to be consistent with those of the corresponding RRM models as much as possible (see Fig. 4a). Note that the virtual RRM models show slight deformations and partial defects, and thus the interactive placement of the virtual fiducials is prone to large artificial errors. The coarse registration (CR) matrix  ${}^P_I T_{coarse}$  represented by the transformation between  $F_p$  and  $F_I$  can be calculated by the singular value decomposition (SVD) algorithm [8]. Then the PPC  $X$  and the IPC  $Y$  can be initially aligned by updating  $X$  to  ${}^{CR}X = \{{}^{CR}x_i\}$ , namely

$${}^{CR}X = {}^P_I T_{coarse} \cdot X \tag{5}$$

**Fine registration using RAMSICP algorithm**

The fine registration matrix  ${}^P_I T_{fine}$  represented by the transformation between  ${}^{CR}X$  and  $Y$  is calculated using the proposed RAMSICP algorithm which is an extension of standard ICP algorithm to avoid falling into a local optimum and wrong registration tendency caused by poor CR and the large asymmetry of  ${}^{CR}X$  and  $Y$  in the number and distribution. Figure 5 shows the basic principle of the RAMSICP algorithm.

The  $k$ -distance neighborhood ( $k$ -DN)  $s_i$  of  ${}^{CR}x_i$  is selected as the matching sub-range, excluding numerous possible disturbances (e.g., outliers or noises) from  $X$ . Define the complete matching range set  $S$  as follows:

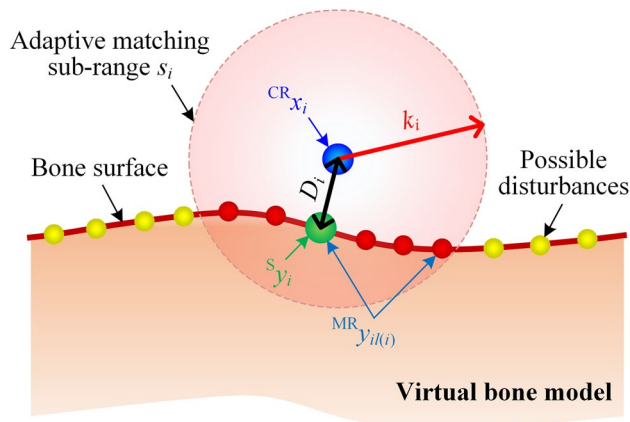


**Fig. 5** Schematic diagram of the RAMSICP algorithm

$$\mathbf{S} = \left\{ s_i \mid |s_i - {}^{\text{CR}}x_i| < k_i \right\} \text{ for } i = 1, \dots, N_p \quad (6)$$

where  $k_i$  represents the size of  $s_i$ . In iterations, only the FPs limited in  $\mathbf{S}$  can participate in registration. Thus,  $\mathbf{Y}$  is updated to  ${}^{\text{MR}}\mathbf{Y} = \{{}^{\text{MR}}y_{i(i)}\}$ , namely

$${}^{\text{MR}}\mathbf{Y} = \mathbf{S} \cap \mathbf{Y} \neq \emptyset \quad (7)$$

Then, Each FP in  ${}^{\text{MR}}\mathbf{Y}$  closest to  ${}^{\text{CR}}x_i$  is searched out to compose the point set  ${}^{\text{S}}\mathbf{Y} = \{{}^{\text{S}}y_i\}$ .  $k_i$  determines the IPC samples in iterations and thus affects the registration accuracy. We assume that whether  $k_i$  is so large that numerous outliers and noises exist in  ${}^{\text{MR}}\mathbf{Y}$  or too small to retain essential FPs in  ${}^{\text{MR}}\mathbf{Y}$ , it is likely to cause mismatches. Consequently, a suitable  $k_i$  seems necessary to minimize the registration error. In this study, considering the various CR results and local distributions of the IPC samples near each FP in the PPC,  $k_i$  is adjusted adaptively by multiplying a positive scale factor  $L_i$  and the Euclidean distance  $D_i$  between the corresponding closest point pairs  ${}^{\text{CR}}x_i$  and  ${}^{\text{S}}y_i$ , namely

$$k_i = L_i \cdot D_i \quad (8)$$

where  $L_i$  is set as a uniform value  $L$  for simplification.

Actually, certain mismatched point pairs may be unavoidable due to the asymmetry of the PPC and the IPC. However, in this study, we disuse the rejection strategy [23] due to the few FPs in the PPC, and omit the weighting process due to the insignificant contribution to the accuracy improvement [31]. The objective function  $d_h$  is defined to iteratively update the current transformation:

$$d_h = \sqrt{\min \sum_{i=1}^{N_p} \left| {}^{\text{S}}\mathbf{Y}_{i,h} - {}^P\mathbf{T}_{\text{fine},h} \cdot {}^{\text{CR}}\mathbf{X}_{i,h} \right|^2} \quad (9)$$

where  $h$  is the iteration number, and  ${}^P\mathbf{T}_{\text{fine}}$  is solved by the SVD method [8]. Iterations are terminated when  $d_{h+1} - d_h < \varepsilon$  where  $\varepsilon$  is set to  $10^{-5}$  mm. Eventually,  ${}^P\mathbf{T}$  can be calculated as follows:

$${}^P\mathbf{T} = {}^P\mathbf{T}_{\text{coarse}} \cdot {}^P\mathbf{T}_{\text{fine}} \quad (10)$$

## Results and discussion

### Experimental preparation

A series of experiments were performed to demonstrate the effectiveness of our proposed CR-RAMSICP in improving the registration accuracy characterized by the TRE, by comparison with that of CR and CR combined with the standard ICP algorithm (termed CR-ICP). First, depending on the planned osteotomy trajectory, a small bone block was resected from the complete isolated porcine ilium using our self-developed ORS (see Fig. 6), and the retained part was used for experiments. Then, follow our aforementioned procedures to acquire FPs. The TRE was computed using four distinct endpoints (see Fig. 6b) on the resected surface of the retained part, which can be expressed mathematically as:

$$\text{TRE} = \sqrt{\frac{1}{4} \sum_{n=1}^4 \left| Y_n - {}^P\mathbf{T} \cdot X_n \right|^2} \quad (11)$$

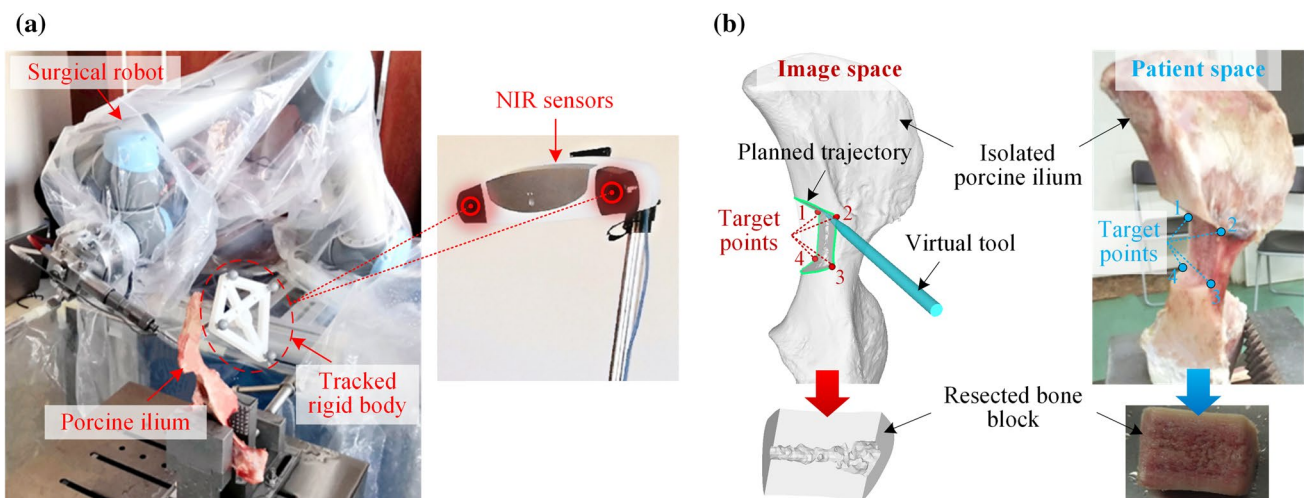


**Fig. 6** **a** Osteotomy scene. **b** Effects of planned and actual osteotomy. The target points in image and patient spaces are marked with red and blue, respectively

where  $X_n$  represents the  $n$ th target point collected by the tracked probe in patient space and  $Y_n$  represents the corresponding one placed interactively in image space. It should be clarified that the operation processes of collecting the target point coordinates were very carefully carried out, and each real target point coordinate was estimated by the mean of the corresponding measured ones in ten repeated measurements.

### Effect of the scale factor

To investigate the impact of the scale factor  $L$  involved in the RAMSICP algorithm on the registration accuracy, FPs located in three different SA combinations (denoted as Combs. 1, 2 and 3) were selected to register with the IPC, respectively. The TRE changes corresponding to Combs. 1, 2 and 3 with different scale factors varying from 1 to 5 are shown in Fig. 7, which first decrease and then increase. Note that an optimal scale factor range  $R_{opt}$  corresponding to the minimum TRE can be reached in each case, but is different in different registrations.

However, it is very difficult to preset an optimal scale factor  $L_{opt}$  located in  $R_{opt}$ . To enhance the fault tolerance of the algorithm, in all subsequent experiments, the reference range (1 to 5) of  $L$  was discretized with an increment  $\Delta L = 0.2$  to calculate the TRE corresponding to each assigned  $L$ , and  $L_{opt}$  that yields the minimum TRE was picked out directly. It should be clearly stated that in this case, the longest calculation time is less than 10 s, far less than that of the whole operation process (about 8–15 min).

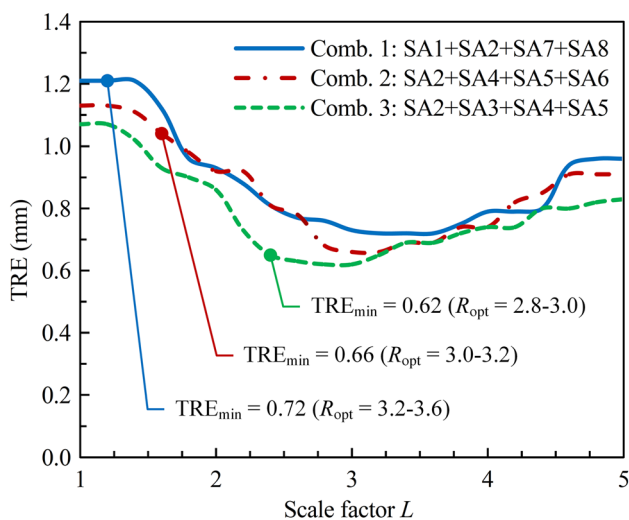


Fig. 7 The TRE changes with the scale factor

### Reproducibility and robustness to different CR errors

- (1) *Reproducibility.* To evaluate the reproducibility of accuracy for the three aforementioned methods, fifteen prepared experimental subjects were registered by different operators, respectively. The corresponding results shown in Fig. 8 indicate that the mean TREs for CR, CR-ICP and CR-RAMSICP are  $1.33 \pm 0.27$  mm,  $0.89 \pm 0.14$  mm and  $0.56 \pm 0.08$  mm, respectively. Obviously, CR-RAMSICP exhibits the lowest mean and standard deviation of the TREs and thus is more accurate and reproducible than CR and CR-ICP.
- (2) *Robustness.* To investigate the robustness of CR-RAMSICP to CR errors, we artificially adjusted the placement deviations of the virtual fiducials to extend the CR error range which was limited within 1 to 5 mm and divided into eight levels (denoted as Levels 1 to 8) with a 0.5 mm interval. For each CR error level, five groups of experiments were performed, and the TREs for CR-RAMSICP and CR-ICP are shown in Fig. 9. The results indicate that the TREs for CR-ICP display a general increasing trend proportional to the CR errors, which are always higher than those for CR-RAMSICP; in contrast, the TREs for CR-RAMSICP are stable within 1 mm under the CR errors at Levels 1 to 6, but sharply increase and gradually tend to approach those for CR-ICP when the CR error is more than 4 mm. In general, compared with CR-ICP, CR-RAMSICP can enhance the robustness to poor CR errors to a certain extent.

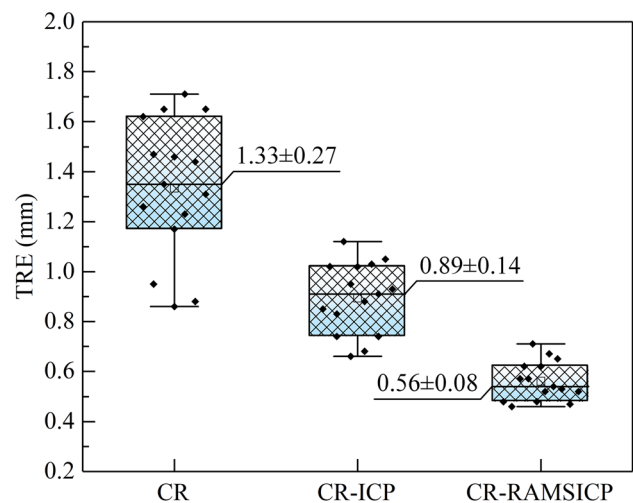
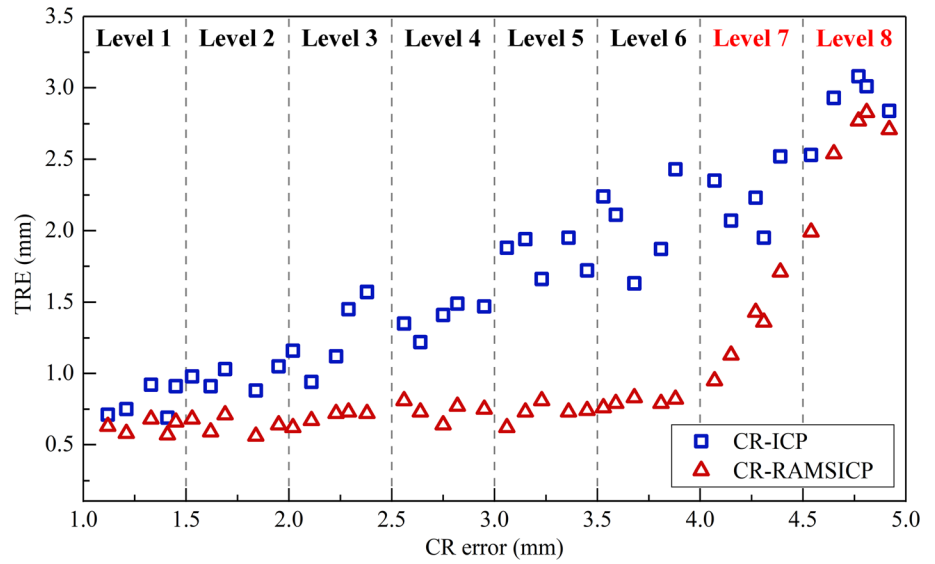


Fig. 8 Comparison of the TREs for different registration methods

**Fig. 9** Comparison of the TREs for CR-RAMSICP and CR-ICP under different CR errors



**Sensitivity to sampling with the tracked probe**

During practical surgical intervention, sampling with the tracked probe is limited by the accessibility of exposed anatomic surfaces, and thus fewer points and more compact sample distribution are expected on the premise of ensuring the accuracy. Therefore, we compared the sensitivity of CR-ICP and CR-RAMSICP to the number and distribution of FPs collected by the tracked probe, respectively.

(1) *Sensitivity to the distribution of FPs collected by the tracked probe.* The only five FPs located in each SA (see Fig. 4c) were separately extracted for registration,

and the experiments were repeated 10 times by different operators. The TREs for different methods under different distributions of FPs collected by the tracked probe are shown in Fig. 10a. The results indicate that SA3, SA4 and SA5 show low TREs, which may be associated with the short distances from the measured target points; however, SA7 and SA8 exhibit high TREs due to the long distances from the target points. Generally, for each SA, the TREs for CR-RAMSICP exhibit lower values and smaller differences than those for CR-ICP.

(2) *Sensitivity to the number of FPs collected by the tracked probe.* 1, 2, 3 and 4 FPs were selected from each SA,

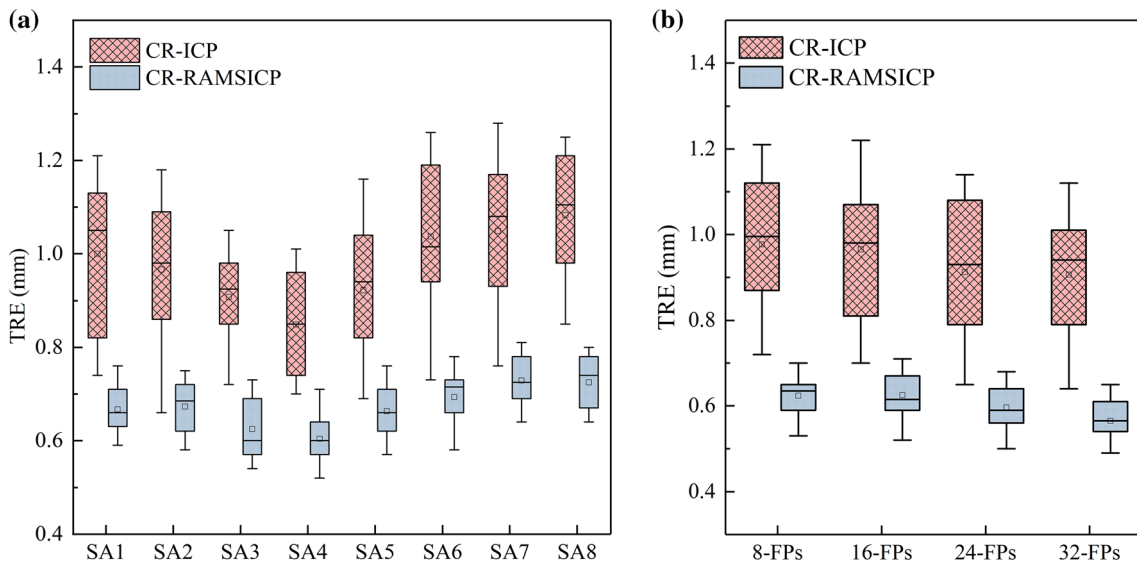


**Fig. 10** Comparison of the TREs for CR-RAMSICP and CR-ICP under different distributions and numbers of FPs collected by the tracked probe. **a** The case for different FP distributions. **b** The case for different FP numbers



respectively; that is, a total of 8, 16, 24 and 32 FPs in patient space were used for registration, respectively. The experiments were repeated 10 times by different operators. The TREs for different methods under different numbers of FPs collected by the tracked probe are shown in Fig. 10b. The results illustrate that the TREs of CR-RAMSICP and CR-ICP decreases with the increase of the number of FPs; however, CR-RAMSICP shows lower TREs and sensitivity to the FP number. Besides, it can be deduced that CR-RAMSICP has the potentials to provide higher accuracy with fewer FPs because, for example, the TREs for CR-RAMSICP with 8 FPs are generally lower and more stable than those for CR-ICP with 32 FPs.

## Conclusion

In this paper, a hybrid feature-based registration method CR-RAMSICP is proposed, which sufficiently meets the required accuracy of 1 mm without invasive bone-implanted markers. Four RRM attached to the tracked rigid body which is rigidly fixed out of the bone with an extending bracket are used for CR, and their centers can be tracked automatically in patient space and placed interactively in image space. The proposed RAMSICP algorithm is adopted for fine registration to precisely match the PPC collected on the bone surfaces by the tracked probe and the IPC extracted from the corresponding CT datasets. It does not require the establishments of complex metrics and models except the point-to-point distance, which is convenient to program. A series of experiments based on isolated porcine iliums were performed to preliminarily verify the effectiveness of CR-RAMSICP in accuracy improvement. The results illustrate that CR-RAMSICP is not only more accurate and reproducible than CR and CR-ICP, but also exhibits better robustness to CR errors, and lower sensitivity to the distribution and number of FPs collected by the tracked probe than CR-ICP. Besides, it should be clarified that when collecting the PPC with the tracked probe, without loss of generality, we avoided the tendency to select rich features on the porcine ilium surfaces, but the relatively smooth areas. Therefore, from this point of view, CR-RAMSICP may provide the clinical potentials to be extended to other types of long bones.

In future work, we will study robust bone surface segmentation and the determination of optimal IPC resolution to further improve the registration accuracy. More practically, the human phantom experiments will be performed to further evaluate the applicability of CR-RAMSICP and provide relevant practical guidelines for clinical trials.

**Acknowledgements** This study was supported by the National Natural Science Foundation of China (Grant Nos. 51875094) and the

Fundamental Research Funds for the Central Universities (Grant Nos. N2003011).

**Authors' contributions** CZ was involved in conceptualization; CZ and YL were involved in methodology; CZ, YL, and YZ were involved in formal analysis and investigation; CZ was involved in validation; CZ was involved in software and visualization; CZ was involved in data curation; CZ was involved in writing—original draft preparation; CZ, YL, and HL were involved in writing—review and editing; YL was involved in funding acquisition; YL and YZ were involved in resources; YL and YZ were involved in project administration; YL, YZ, and HL were involved in supervision.

**Funding** This study was supported by the National Natural Science Foundation of China (Grant Nos. 51875094) and the Fundamental Research Funds for the Central Universities (Grant Nos. N2003011).

**Availability of data and material** All experimental data in this study are included in this article.

## Declarations

**Conflicts of interest** The authors declare that they have no conflicts of interest.

**Consent to participate** Informed consent was obtained from all individual participants included in the study.

**Ethics approval** This article does not contain any study with human participants or animals performed by any of the authors.

## References

1. Billings S, Kang HJ, Cheng A, Boctor E, Kazanzides P, Taylor R (2015) Minimally invasive registration for computer-assisted orthopedic surgery: combining tracked ultrasound and bone surface points via the P-IMLOP algorithm. *Int J Comput Assist Radiol Surg* 10(6):761–771. <https://doi.org/10.1007/s11548-015-1188-z>
2. Picard F, Deakin AH, Riches PE, Deep K, Baines J (2019) Computer assisted orthopaedic surgery: past, present and future. *Med Eng Phys* 72:55–65. <https://doi.org/10.1016/j.medengphy.2019.08.005>
3. Wang J, Shen Y, Yang S (2019) A practical marker-less image registration method for augmented reality oral and maxillofacial surgery. *Int J Comput Assist Radiol Surg* 14(5):763–773. <https://doi.org/10.1007/s11548-019-01921-5>
4. Chen L, Zhang F, Zhan W, Gan M, Sun L (2020) Research on the accuracy of three-dimensional localization and navigation in robot-assisted spine surgery. *Int J Med Robotics Comput Assist Surg* 16(2):e2071. <https://doi.org/10.1002/rcs.2071>
5. Omara AI, Wang M, Fan Y, Song Z (2014) Anatomical landmarks for point-matching registration in image-guided neurosurgery. *Int J Med Robotics Comput Assist Surg* 10(1):55–64. <https://doi.org/10.1002/rcs.1509>
6. Dong Y, Zhang C, Ji D, Wang M, Song Z (2019) Regional-surface-based registration for image-guided neurosurgery: effects of scan modes on registration accuracy. *Int J Comput Assist Radiol Surg* 14(8):1303–1315. <https://doi.org/10.1007/s11548-019-01990-6>
7. Fanti Z, Torres F, Hazan-Lasri E, Gastelum-Strozzi A, Ruiz-Huerta L, Caballero-Ruiz A, Cosío FA (2018) Improved surface-based registration of CT and intraoperative 3D ultrasound of

- bones. *J Healthc Eng* 2018:1–11. <https://doi.org/10.1155/2018/2365178>
8. Li Q, Song R, Ma X, Liu X (2018) A robust registration algorithm for image-guided surgical robot. *IEEE Access* 6:42950–42960. <https://doi.org/10.1109/ACCESS.2018.2853601>
  9. Zhou C, Anschuetz L, Weder S, Xie L, Caversaccio M, Weber S, Williamson T (2016) Surface matching for high-accuracy registration of the lateral skull base. *Int J Comput Assist Radiol Surg* 11(11):2097–2103. <https://doi.org/10.1007/s11548-016-1394-3>
  10. Maurer CR, Fitzpatrick JM, Wang MY, Galloway RL, Maciunas RJ, Allen GS (1997) Registration of head volume images using implantable fiducial markers. *IEEE Trans Med Imaging* 16(4):447–462. <https://doi.org/10.1109/42.611354>
  11. Chen X, Xu L, Wang H, Wang F, Wang Q, Kikinis R (2017) Development of a surgical navigation system based on 3D Slicer for intraoperative implant placement surgery. *Med Eng Phys* 41:81–89. <https://doi.org/10.1016/j.medengphy.2017.01.005>
  12. Chen X, Ye M, Lin Y, Wu Y, Wang C (2009) Image guided oral implantology and its application in the placement of zygoma implants. *Comput Med Prog Bio* 93(2):162–173. <https://doi.org/10.1016/j.cmpb.2008.09.002>
  13. Lin Q, Yang R, Cai K, Si X, Chen X, Wu X (2016) Real-time automatic registration in optical surgical navigation. *Infrared Phys Techn* 76:375–385. <https://doi.org/10.1016/j.infrared.2016.03.011>
  14. Kaushik A, Dwarakanath TA, Bhutani G (2020) Robust marker detection and high precision measurement for real-time anatomical registration using Taguchi method. *Int J Med Robotics Comput Assist Surg* 16(4):e2102. <https://doi.org/10.1002/rcs.2102>
  15. Arun KS, Huang TS, Blostein SD (1987) Least-squares fitting of two 3-D point sets. *IEEE Trans Pattern Anal Mach Intell PAMI-9*(5):698–700. <https://doi.org/10.1109/TPAMI.1987.4767965>
  16. Dobbe JGG, Curnier F, Rondeau X, Streekstra GJ (2015) Precision of image-based registration for intraoperative navigation in the presence of metal artifacts: application to corrective osteotomy surgery. *Med Eng Phys* 37(6):524–530. <https://doi.org/10.1016/j.medengphy.2015.03.008>
  17. Cho JY, Yang JY, Lee MS, Kwon DS (2011) Verification of registration method using a 3D laser scanner for orthopedic robot systems. In: 2011 11th International Conference on Control, Automation and Systems, pp 460–464
  18. Niu K, Homminga J, Sluiter VI, Sprengers A, Verdonshot N (2018) Feasibility of A-mode ultrasound based intraoperative registration in computer-aided orthopedic surgery: a simulation and experimental study. *PLoS ONE* 13(6):e0199136. <https://doi.org/10.1371/journal.pone.0199136>
  19. Bow H, Yang X, Chotai S, Feldman M, Yu H, Englot DJ, Miga MI, Pruthi S, Dawant BM, Parker SL (2020) Initial experience with using a structured light 3D Scanner and image registration to plan bedside subdural evacuating port system placement. *World Neurosurg* 137:350–356. <https://doi.org/10.1016/j.wneu.2020.01.203>
  20. Jiang L, Zhang S, Yang J, Zhuang X, Zhang L, Gu L (2015) A robust automated markerless registration framework for neurosurgery navigation. *Int J Med Robotics Comput Assist Surg* 11(4):436–447. <https://doi.org/10.1002/rcs.1626>
  21. Digioia AM, Simon DA, Jarama B, Blackwel M, Morgan E, O'Toole RV, Colgan B, Kischel E (1995) HipNav: Pre-operative planning and intra-operative navigational guidance for acetabular implant placement in total hip replacement surgery. *Proc Computer Assisted Orthopaedic Surgery Symp*, Bern, Switzerland, November, 1995
  22. Besl PJ, McKay ND (1992) A method for registration of 3-D shapes. *IEEE Trans Pattern Anal and Mach Intell* 14(2):239–256. <https://doi.org/10.1109/34.121791>
  23. Tazir ML, Gokhool T, Checchin P, Malaterre L, Trassoudaine L (2018) CICIP: Cluster Iterative Closest Point for sparse-dense point cloud registration. *Robot Auton Syst* 108:66–86. <https://doi.org/10.1016/j.robot.2018.07.003>
  24. Wu Z, Chen H, Du S, Fu M, Zhou N, Zheng N (2019) Correntropy based scale ICP algorithm for robust point set registration. *Pattern Recogn* 93:14–24. <https://doi.org/10.1016/j.patcog.2019.03.013>
  25. Jian B, Vemuri BC (2011) Robust point set registration using Gaussian mixture models. *IEEE Trans Pattern Anal Mach Intell* 33(8):1633–1645. <https://doi.org/10.1109/TPAMI.2010.223>
  26. Cutter JR, Styles IB, Leonardis A, Dehghani H (2016) Image-based registration for a neurosurgical robot: comparison using iterative closest point and coherent point drift algorithms. *Proc Computer Sci* 90:28–34. <https://doi.org/10.1016/j.procs.2016.07.006>
  27. Grayeli AB, Esquia-Medina G, Nguyen Y, Mazalaigue S, Vellin J, Lombard B, Kalamarides M, Ferrary E, Sterkers O (2009) Use of anatomic or invasive markers in association with skin surface registration in image-guided surgery of the temporal bone. *Acta Otolaryngol* 129(4):405–410. <https://doi.org/10.1080/00016480802579025>
  28. Stoll KE, Miles JD, White JK, Punt SEW, Conrad EU, Ching RP (2015) Assessment of registration accuracy during computer-aided oncologic limb-salvage surgery. *Int J Comput Assist Radiol Surg* 10(9):1469–1475. <https://doi.org/10.1007/s11548-014-1146-1>
  29. Kong L, Cao L, Zhou Y, Pei Y, Guo S, Fu J, Liu L, Guo Z, Liu H (2017) Development of an image-guided surgical robot for bone tumor resection. In: 2017 IEEE International Conference on Robotics and Biomimetics, pp 2490–2495.
  30. Otsu N (1979) A threshold selection method from gray-level histograms. *IEEE Trans Syst Man Cybern* 9(1):62–66. <https://doi.org/10.1109/TSMC.1979.4310076>
  31. Donoso FA, Austin KJ, Mcaree PR (2017) How do ICP variants perform when used for scan matching terrain point clouds? *Robot Auton Syst* 87:147–161. <https://doi.org/10.1016/j.robot.2016.10.011>

**Publisher's Note** Springer Nature remains neutral with regard to jurisdictional claims in published maps and institutional affiliations.